npj | microgravity

Article

Published in cooperation with the Biodesign Institute at Arizona State University, with the support of NASA

https://doi.org/10.1038/s41526-025-00499-4

Theoretical investigation of an atomic Fabry Perot interferometer based acceleration sensor for microgravity environments

Check for updates

Manju Perumbil[1,2] ✉, Matthew J. Blacker[2,3], Stuart S. Szigeti[2] & Simon A. Haine[2]

We investigate the use of an atomic Fabry-Perot interferometer (FPI) with a pulsed non-interacting Bose-Einstein condensate (BEC) source as a space-based acceleration sensor. We derive an analytic approximation for the device's transmission under a uniform acceleration, which we use to compute the device's attainable acceleration sensitivity using the classical Fisher information. In the ideal case of a high-finesse FPI and an infinitely narrow momentum width atomic source, we find that when the device length is limited, the atomic FPI can achieve greater acceleration sensitivity than a Mach-Zender (MZ) interferometer of equivalent device length. Under the more realistic case of a finite momentum width source, we identify the ideal cavity length for the best sensitivity. Although the MZ interferometer now offers enhanced sensitivity within currently achievable parameter regimes, our analysis demonstrates that the atomic FPI holds potential as a promising future alternative if narrow momentum width atomic sources can be engineered.

The existing generation of atom interferometers have provided state-of-the-art measurements of accelerations[1,2], rotations[3–7], gravitational fields[8–14], gravity gradients[15–20], the fine structure constant[21–23], and Newton's gravitational constant[24]. With sufficient miniaturisation and ruggedization, quantum sensors based on atom interferometry could enable new capabilities in navigation[25–30], civil engineering risk management[31–33], mineral exploration and recovery[34,35], groundwater mapping and monitoring[36], and geodesy[37–40]. Atom interferometers are presently being developed for mobile operation on dynamic platforms, and have been deployed on ships[41,42], aircraft[43–45], and in microgravity environments onboard sounding rockets[46,47] and the International Space Station[48]. Spaceborne operation in particular has provided a strong motivation for next-generation atom-interferometric development, since it could progress key questions in fundamental physics through low-frequency-band gravitational wave detection[49], weak equivalence principle violation tests[50,51], and novel experiments into dark energy[52,53], dark matter[54,55], and quantum gravity[56,57]. Recent advancements in space-based atom interferometry have demonstrated its potential for high-precision gravitational measurements, significantly enhancing satellite geodesy and Earth observation[40,58,59]

There is a worldwide effort to decrease the size, weight, and power (SWaP) of atomic inertial sensors whilst maintaining sensitivity, accuracy, and stability on dynamic platforms in real-world environments[27,35,60,61]. Efforts to address these challenges have largely focussed on improving the performance of the standard three-pulse Mach-Zehnder (MZ) atom interferometer, through innovations such as large momentum transfer atom optics[62–69], improved atomic source quality and production rate[70–76], novel state readout[77–79], error-robust quantum control[80–84], and overcoming the shot-noise limit through quantum entanglement generated from atom-atom[85–94] or atom-light[95–103] interactions. However, another approach is to consider alternatives to the standard MZ atom interferometer, which could relax certain technological requirements and provide advantages in tight-SWaP situations.

One alternative interferometry configuration is the atomic analogue of a Fabry-Perot interferometer (FPI). In an optical FPI, light enters a cavity formed by two parallel mirrors, and a resonant spectra is obtained by scanning the incident wavelength. Optical FPIs have been extensively used in a number of spectroscopic[104–106] and sensing[107,108] applications. In an atomic FPI, the incoming light is replaced by atomic matter-waves and the

[1]ITEP, Department of Education, Central University of Kerala, Kasaragod, Kerala, India. [2]Department of Quantum Science and Technology, The Australian National University, Research School of Physics, Canberra, ACT, Australia. [3]Department of Applied Mathematics and Theoretical Physics, University of Cambridge, Cambridge, UK. ✉e-mail: manjuperumbil@cukerala.ac.in

mirrors are replaced by laser-induced potential barriers. Previous theoretical studies into atomic FPIs have demonstrated that an ultracold Bose source can produce high contrast Fabry-Perot interference fringes[109–113], characterised their resonance properties[114,115], and investigated the potential use of atomic FPIs in velocity selection[116,117] and angle selection[118]. For the experimental regimes achievable with current technology, a narrow momentum width source such as a Bose-Einstein condensate (BEC) is needed to achieve the high contrast resonant transmission peaks required for useful sensing[119]. Operating in a regime where atom-atom collisional interactions are negligible is also highly desirable, and can be obtained through a Feshbach resonance[120–122]. The suitability of a noninteracting BEC source for atomic Fabry-Perot interferometry has been validated in a recent experimental demonstration using a ^{39}K BEC source and optical barrier potentials formed using a digital micromirror device[123].

In this paper, we study the application of an atomic FPI as an acceleration sensor. A previous work has considered the suitability of atomic FPIs for gravimetry through a numerical simulation analysis[124]. Here we take a complementary analytic approach that aims to give deeper insights into the optimal parameter regime and performance limits of an atomic FPI acceleration sensor. This approach allows us to assess whether there are regimes where an atomic FPI could potentially offer superior performance as an acceleration sensor compared to MZ interferometry. We are particularly interested in situations where device size is highly constrained, such as in space-based applications. Since we are interested in fundamental performance limits, we consider only the case of a non-interacting BEC in this work.

Specifically, in Section "Methods" we derive an analytic expression for the transmission of a non-interacting BEC through the atomic FPI in an accelerating field, which we validate by numeric simulation of the Schrödinger equation for N non-interacting particles. We first study in Section "Acceleration sensitivity of an atomic FPI with a plane matter-wave input" the ideal case of an infinitely narrow momentum width source, and from the transmission derive an approximate expression for the optimum Fisher information (and consequently acceleration sensitivity). We then consider in Sections "Space-Based Accelerometer Using a BEC With a Finite Momentum Width" and "Optimising Cavity Length and Corresponding Acceleration Sensitivity for a Particular Momentum Width" atomic clouds with a finite momentum width, and study the effect of finite momentum width upon the free parameters which lead to optimal Fisher information. In each case, in Sections "Comparing Acceleration Sensitivities of an Atomic FPI and a MZ Interferometer" and "Comparing Sensitivities of a MZ Interferometer and an Atomic FPI" respectively we compare the acceleration sensitivity of a space-based atomic FPI to a space-based MZ interferometer of equivalent device size, to assess the future potential of an atomic FPI as an alternative accelerometry device.

Results

Acceleration sensitivity of an atomic FPI with a plane matter-wave input

We begin our investigation into the sensitivity of an atomic FPI as an accelerometer by considering a BEC source with an infinitely narrow momentum width. This provides intuition for parameter dependencies of the sensitivity in the ideal case which optimises transmission through the FPI[119].

At first we vary the momentum kick $\tilde{k}_i$ given to the cloud and calculate the classical Fisher information for each case as shown in Fig. 1. F_C varies with $\tilde{k}_i$ which is shown in Fig. 1 for different cavity lengths. The sharp peaks correspond to the point where transmission coefficient $T \approx 1$, the reason for which is discussed in detail in Section "Space-Based Accelerometer Using a BEC With a Finite Momentum Width". From Fig. 1 we can estimate the optimum $\tilde{k}_i$ that gives the maximum F_C (optimum F_C) for each cavity length.

Figure 2a shows the variation in optimum $\tilde{k}_i$ as a function of the cavity length (the height of the first barrier is fixed here, resulting in a constant κ). Here we can see that as the cavity length increases, optimum $\tilde{k}_i$ decreases. This means that, for a fixed barrier height, the optimum momentum of the atoms that gives maximum sensitivity to acceleration decreases with increasing cavity length.

Figure 2b illustrates the variation in $\tilde{F}_C$ corresponding to optimum $\tilde{k}_i$ as a function of cavity length. This shows that F_C and hence the sensitivity increases with increasing cavity length in the case of a cloud with infinitely narrow momentum width.

The trend in Fig. 2 arises due to the changes in transmission peak properties with variation in the cavity length. As the cavity length increases, the linewidth of the resonant peaks gets narrower, leading to curves with higher slopes ($\partial T/\partial k$)[119]. The relationship between the slope of the transmission spectra and acceleration sensitivity can be obtained as follows. Under uniform acceleration, the velocity of the cloud at the position of the first barrier is $v = v_0 + at$, where v_0 is the initial velocity, t is the time taken to reach the first barrier and a is the acceleration. This yields

$$\frac{\partial T}{\partial a} = \frac{\partial T}{\partial k}\frac{\partial k}{\partial a} = \frac{mt}{\hbar}\frac{\partial T}{\partial k}. \tag{1}$$

Equations (27) and (1) show that the classical Fisher information increases with increasing $\partial T/\partial k$. Hence, as the cavity length increases, an increase in the slope ($\partial T/\partial k$) causes the increase in F_C, as observed in Fig. 2b. Here, the time t depends on the distance between the initial position of the cloud and the position of the first barrier L. Hence, the sensitivity depends on L.

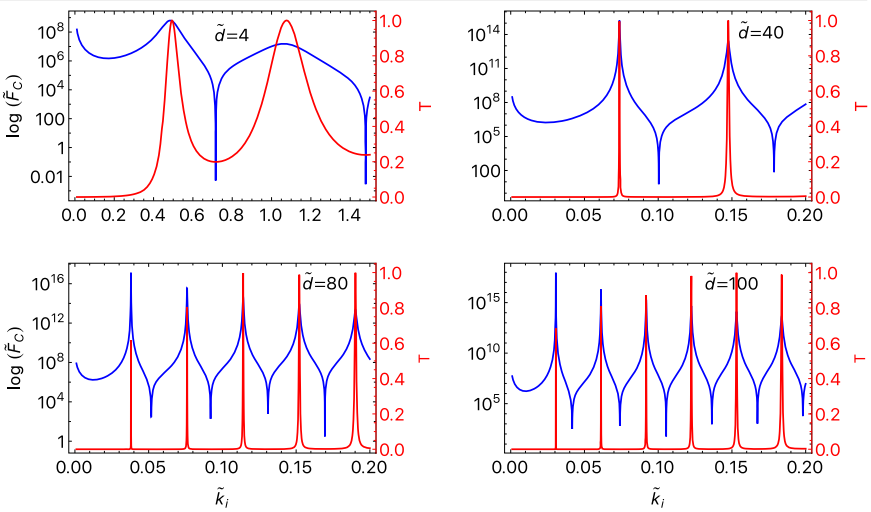

Fig. 1 | The classical Fisher information (F_C), in the case of an infinitely narrow momentum width source of atoms, is plotted (black curves) as a function of the wave vector of atomic cloud (The dimensionless wave vector, $\tilde{k}_i = k_i/\kappa$, where $\kappa = \sqrt{(2mV_1/\hbar)}$ is the wave vector corresponding to the characteristic energy of the first barrier). The red curves illustrates the variation in transmission coefficient T. Here, κ is kept constant and k_i is varied for different cavity lengths d. The peaks in F_C are shown to correspond to the transmission resonant peaks. The optimum $\tilde{k}_i$ that gives the highest value of F_C can be calculated from this plot. It shows that the optimum F_C and $\tilde{k}_i$ varies with cavity length.

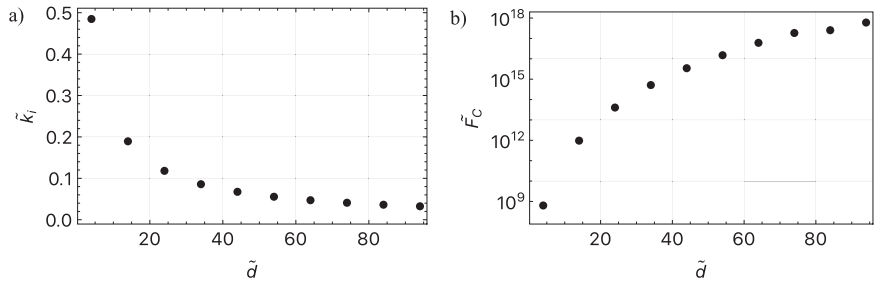

Fig. 2 | Cavity length dependence of optimal momentum and Fisher information for an infinitely narrow momentum-width source. Optimum particle momentum (**a**) and the Fisher information corresponding to the optimum particle momentum (**b**) as a function of the cavity length, in the case of an infinitely narrow momentum width source of atoms. For each cavity length there exists an optimum $\tilde{k}_i$ and it decreases with increasing cavity length. The optimum value of $\tilde{k}_i$ ranges from 0.06 to 0.004 k_0, where $k_0 = 2\pi/(780\text{nm})$. The maximum $\tilde{F}_C$ increases with increasing cavity length. Hence in this case, sensitivity to acceleration can be improved by increasing cavity length.

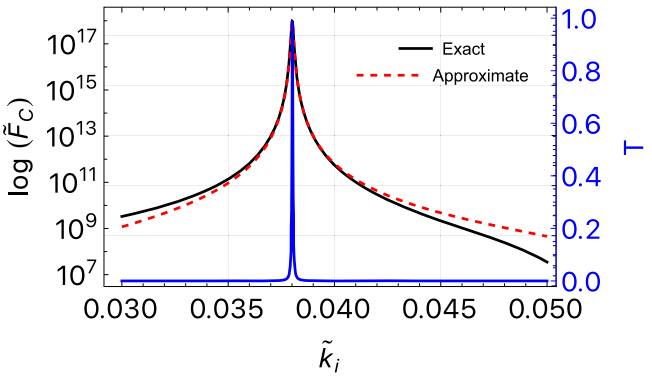

Fig. 3 | Comparison of the variation of $\tilde{F}_C$ with $\tilde{k}_i$ using exact (equation (27)-dimensionless form) and approximate (equation (2)) expressions of $\tilde{F}_C$ in the black and red dashed curve respectively. The blue curves illustrates the variation in transmission coefficient (T). The approximate value of optimum $\tilde{F}_C$ agrees well with the exact value near the optimum region. Here, $\tilde{d} = 80$ and $\tilde{a} \to 0$.

We now formulate a compact analytic expression for the classical Fisher information that is straightforward to optimise, thereby providing a 'best-case' estimate of an atomic FPI accelerometer's sensitivity. For an infinitely narrow source, we obtain the Fisher information by substituting Eq. (15) into Eq. (27). In calculating $\partial T/\partial a$, we assume the dependence on acceleration of finesse $\mathcal{F}$ and phase ϕ_a is insignificant compared to the dependence on acceleration of k. Under that assumption, we obtain

$$\tilde{F}_C^{\text{approx}} = \frac{16\tilde{d}^2\mathcal{F}^4\pi^2 T_{\max}\sin^2(2\Phi(\tilde{a}))\left(\frac{\partial\tilde{k}(\tilde{a})}{\partial\tilde{a}}\right)^2}{\left(\pi^2(T_{\max}-1)-4\mathcal{F}^2\sin^2(\Phi(\tilde{a}))\right)\left(\pi^2+4\mathcal{F}^2\sin^2(\Phi(\tilde{a}))\right)^2}, \tag{2}$$

where

$$\Phi(\tilde{a}) = \phi_a + \tilde{k}(\tilde{a})\tilde{d}, \tag{3a}$$

In Fig. 3, we compare this approximate expression (red dashed curve) to the exact expression (black curve) computed numerically via Eq. (27). In the region near the optimum (maximum) $\tilde{F}_C$, the curves agree very well, validating the approximate expression in Eq. (2).

We now derive an expression for this optimum F_C, and hence the precision to which the acceleration can be inferred. We assume that the acceleration is known ~($a \approx a_0$), and we wish to determine small deviations δa from this value. That is $a = a_0 + \delta a$. We assume that

1. $T_{\max} \approx 1$ in an optimal parameter regime, as motivated by the results of Fig. 10;
2. The optimum $\tilde{F}_C$ corresponds to the position of the resonant transmission peak $T_{\max} \approx 1$, as shown in Fig. 5a). From Eq. (15), this approximation corresponds to $\Phi(a) = n\pi$ for $n \in \mathbb{Z}$.

In the limit $\delta a_0 \to 0$, we obtain

$$\tilde{F}_{C_{\text{opt}}} = \frac{4\tilde{d}^2\mathcal{F}^2\tilde{L}^2}{(\tilde{k}_i^2 + \tilde{a}_0\tilde{L})\pi^2}. \tag{4}$$

Converting back to dimensional form gives

$$F_{C_{\text{opt}}} = \frac{16m^4d^2\mathcal{F}^2L^2}{\hbar^4\pi^2\left[k_i^2 + \frac{2m^2La_0}{\hbar^2}\right]}. \tag{5}$$

This is a key result of this paper, and can be used to efficiently determine the fundamental acceleration sensitivity attainable by an atomic FPI.

Comparing acceleration sensitivities of an atomic FPI and a MZ interferometer

Having obtained an expression for the optimal Fisher information for atomic FPI, we may now compare that result with the optimum sensitivity of a MZ interferometer of equivalent interferometer length, since total device length is the limiting constraint for many real-world applications. For concreteness, we consider space-based accelerometry, which is a particularly tight-SWaP deployment environment.

For a space-based system, we can approximate $a_0 = 0$, and hence the $F_{C_{\text{opt}}}$ and optimum sensitivity per particle of an atomic FPI can be found from eqs. (25) and (5):

$$F_{C_{\text{opt}}} = \frac{16m^4d^2\mathcal{F}^2L^2}{\hbar^4\pi^2k_i^2}, \tag{6a}$$

$$\delta a_{\text{FPI}} = \frac{1}{\sqrt{F_{C_{\text{opt}}}}} = \frac{k_i\pi\hbar^2}{4m^2d\mathcal{F}L}. \tag{6b}$$

In the case of a MZ interferometer, the per particle sensitivity is given by[9]

$$\delta a_{\text{MZ}} = \frac{1}{k_i\mathbb{T}^2}, \tag{7}$$

where k_i is the effective momentum transferred to the atoms by the beamsplitters of the interferometer. The total interferometer time, $2\mathbb{T}$ is

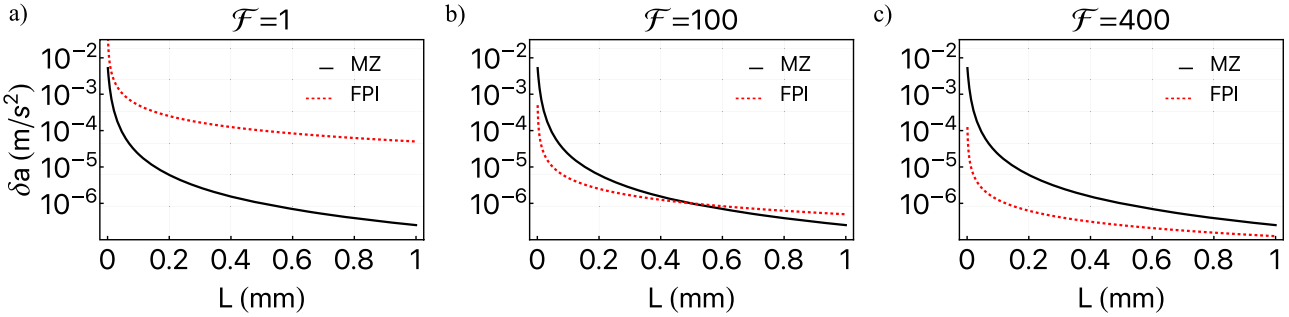

Fig. 4 | Plots comparing the acceleration sensitivities of a space-based ($a_0 \to 0$) MZ interferometer (black curve) and an atomic FPI (red dashed curve) with $k_i = 0.0596k_0$, $w = 1$ μm and $d = 4$ μm. Here the minimum change in acceleration that can be detected, δa, is plotted as a function of length L, for varying finesse values (**a**) $\mathcal{F} = 1$, (**b**) $\mathcal{F} = 100$ and (**c**) $\mathcal{F} = 400$. L is the initial distance between the BEC and the first barrier in an atomic FPI. For a MZ interferometer, the total interferometer length $L_t = L + 2w + d$. A particular finesse can be achieved while varying L, by manipulating barrier height accordingly. The sensitivity of an atomic FPI is better than that of the comparison MZ interferometer for high finesse and low length scales.

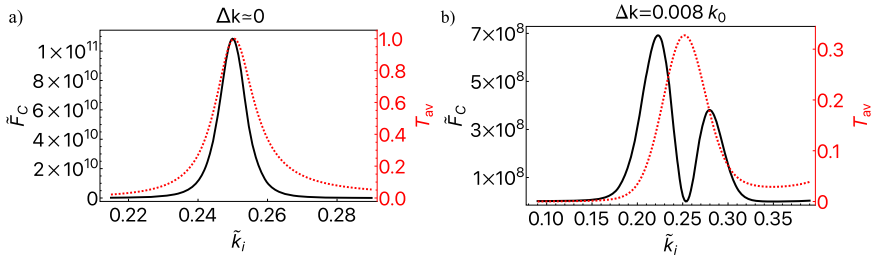

Fig. 5 | Effect of source momentum width on transmission and Fisher information. Transmission coefficient (red dashed curve) and classical Fisher information (black curve) are plotted as a function of the atomic wave vector, (**a**) for an infinitely narrow momentum width atomic cloud and (**b**) for a finite momentum width atomic cloud. The optimum $\tilde{F}_C$ is positioned almost at the $\tilde{k}_i$ corresponding to the transmission peak in the first case. However, it deviates from the transmission peak point when the cloud has a finite momentum width. Here, $k_0 = 2\pi/(780\text{ nm})$.

constrained to

$$\mathbb{T} = \frac{L_t}{v}, \tag{8}$$

where $v = \hbar k_i/m$ is the velocity of the atoms when $a_0 \to 0$, and L_t is the total length of the interferometer. For a fair comparison, we set L_t to the same total length as the atomic FPI: $L_t = L + 2w + d$. Substituting these into Eq. (7) gives

$$\delta a_{\mathrm{MZ}} = \frac{\hbar^2 k_i}{m^2(L + 2w + d)^2}. \tag{9}$$

We can see immediately that making the device size L_t smaller results in poorer sensitivity for both a MZ interferometer and an atomic FPI. However, Eqs. (6b) and (9) show that the scaling of sensitivity with device length is different in each case. We are therefore motivated to study the variation of sensitivity δa with length L, which we show for a range of finesse values $\mathcal{F}$ in Fig. 4. Here optimum values are used for k_i, w and d[119]. For low length ($L < 0.4$ mm) and high finesse ($\mathcal{F} > 100$), the fundamental sensitivity of an atomic FPI surpasses that of a MZ interferometer.

Space-based accelerometer using a BEC with a finite momentum width

Having compared an atomic FPI to a MZ interferometer for the ideal case of infinitely narrow momentum width, we now consider the more realistic case of finite momentum width. This immediately presents a new challenge: if this finite momentum width is greater than the cavity linewidth, only a portion of the atomic cloud (in momentum space) is on resonance and gets transmitted. This reduces the resonant transmission (i.e., $T_{\max} < 1$), so in order to achieve complete resonant transmission (i.e., $T_{\max} = 1$) we are immediately restricted to cavities with linewidth greater than the finite momentum width of the cloud. As linewidth decreases as cavity width increases, this puts an upper bound on the cavity width for an effective atomic FPI[119]. For the cloud of finite momentum width, we consider a Gaussian of full width at half maximum (FWHM) of $\Delta k = 0.008k_0$, where here $k_0 = 2\pi/(780\text{ nm})$. Note that $\Delta k = 2\sqrt{2\ln 2}/\sigma_c$, where $\sigma_c/\sqrt{2}$ is the standard deviation of the Gaussian density profile, or equivalently a Gaussian k-space density profile with standard deviation $1/(\sqrt{2}\sigma_c)$.

With that in mind, we now study how the atomic cloud's finite momentum width affects the dependence of the optimal Fisher information $\tilde{F}_C$ on the initial momentum kick $\tilde{k}_i$ and cavity width $\tilde{d}$. In Fig. 5, we plot $\tilde{F}_C$ as a function $\tilde{k}_i$ for an atomic cloud with infinitely narrow and finite momentum width in Fig. 5a, b respectively. We use the parameters $w\kappa = 1$, $w = 1$ μm and $\kappa = 0.124\,k_0$, as determined in ref. 119.

In Fig. 5b, we demonstrate that for a finite momentum width source, the location of the optimum Fisher information $\tilde{F}_C$ shifts to no longer coincide with the location of the transmission peak. $\tilde{F}_C$ is now relatively small at the position of $T_{\max}$, and the optimum $\tilde{F}_C$ is shifted to a point where the slope of the resonance curve is non-zero. To explain this shift, lets first consider why the peak is at zero acceleration in the case of an infinitely narrow momentum-width source. As the transmission can be tuned to precisely 100% (at $a = 0$) in this case, the *reflection* coefficient is precisely zero, and thus a small acceleration causes a change in the reflection coefficient with high signal to noise ratio. This is analogous to how the optimum operating point in an optical Michelson interferometer is close to the dark port[125]. This is easy to see by recalling Eq. (27):

$$F_C(a) = \frac{(\partial T/\partial a)^2}{T(a)} + \frac{(\partial T/\partial a)^2}{1 - T(a)}. \tag{10}$$

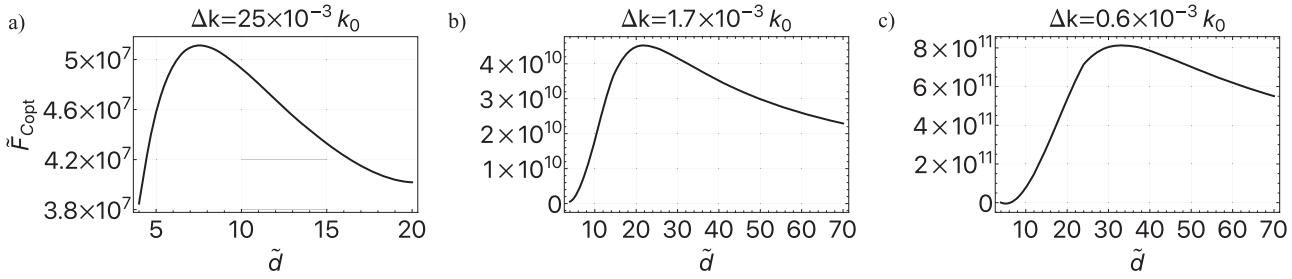

Fig. 6 | Optimum value of $\tilde{F}_C$ as a function of cavity length, for different momentum widths. $\tilde{F}_{C_{opt}}$ increases up to a maximum value and then decreases with increasing cavity length. The optimum cavity length which gives $\tilde{F}_{C_{opt}}$ varies with the momentum width. Here, $k_0 = 2\pi/(780\text{ nm})$.

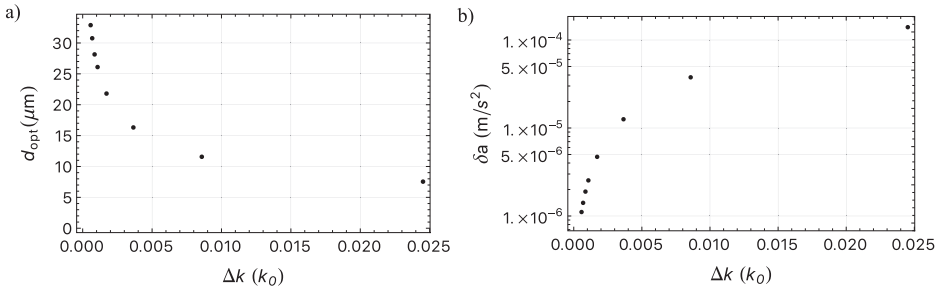

Fig. 7 | Dependence of optimum cavity length and acceleration sensitivity on source momentum width. a Plot showing the optimum value of the cavity length (which gives maximum F_C) as a function of the momentum width of the BEC source. The optimum cavity length decreases with increasing momentum width. **b** Minimum detectable change in acceleration, δa decreases with decreasing momentum width of the BEC source. Hence acceleration sensitivity improves with decreasing momentum width. Here, $k_0 = 2\pi/(780\text{ nm})$.

Around the transmission peak point, the curve can be approximated as a quadratic,

$$T(a) = T_{\max}(1 - Ca^2), \tag{11}$$

where C is a constant. Under a uniform acceleration, k and a have a roughly linear relationship, so at the transmission peak $T_{\max}$ the derivative $\partial T/\partial a \propto \partial T/\partial k \approx 0$. For an infinitely narrow momentum width source, $T_{\max} = 1$, so the denominator in the Fisher information $T(1-T) = 0$. Then,

$$\lim_{a\to 0} F_C = \frac{0}{1} + \lim_{a\to 0}\frac{(-2Ca)^2}{Ca^2} = 4C. \tag{12}$$

Hence, F_C converges to a finite value. However, a source with non-zero momentum width has $T_{\max} < 1$, so only the numerator approaches zero and $F_C \to 0$ at the transmission peak. Thus, the peak Fisher information does not coincide with the transmission peak; so for a finite momentum width source, we have to numerically determine the parameter regime which optimises F_C.

Optimising cavity length and corresponding acceleration sensitivity for a particular momentum width

As before, we calculate the Fisher information $\tilde{F}_C$ as a function of initial momentum kick $\tilde{k}_i$ for a range of cavity widths $\tilde{d}$ and momentum widths $\Delta k = 2\sqrt{2\ln 2}/\sigma_c$ which gives a maximum $\tilde{F}_C$. For each cavity length there is an optimum $\tilde{k}_i$ corresponding to the optimum Fisher information $\tilde{F}_C$ and this optimum point changes with cavity length. However, the optimum $\tilde{k}_i$ is not changed by variation in the momentum width Δk. This is because the optimum initial momentum kick $\tilde{k}_i$ depends upon the location of the first resonant peak, which is independent of the momentum width of the source. However, the momentum width Δk does affect the height of the transmission peak, and therefore the optimum $\tilde{F}_C$[119]. We thus plot the maximum $\tilde{F}_C$ that occurs at the optimum $\tilde{k}_i$ as a function of cavity width $\tilde{d}$ in Fig. 6 for different source momentum widths Δk.

Unlike in the infinitely narrow momentum width case (see Fig. 2a), there is not an unbounded increase in the optimum Fisher information $\tilde{F}_C$ with cavity width $\tilde{d}$. Rather, $\tilde{F}_C$ reaches a maximum and then decreases after the cavity width $\tilde{d}$ exceeds an optimal value. This optimal value arises because the cavity linewidth decreases as the cavity width increases[119]. When the cavity width $\tilde{d}$ exceeds the optimal value, the corresponding linewidth becomes smaller than the momentum width Δk, and (as discussed earlier) transmission through the atomic FPI is suppressed and the optimal Fisher information $\tilde{F}_{C_{opt}}$ decreases.

Equivalently, as the momentum width increases, a larger linewidth (and smaller cavity width) is needed for complete transmission. That is, the peak in Fisher information $\tilde{F}_C$ occurs at a smaller cavity width. This trend is illustrated in Fig. 7a, where we plot the cavity width d corresponding to the maximum optimal Fisher information against the momentum width Δk.

We also find in Fig. 6 that the maximum optimal Fisher information decreases as the momentum width increases. This is because, as shown in ref. 119, resonant transmission is suppressed and transmission peaks broaden as momentum width Δk increases. A decrease in Fisher information corresponds to a worse sensitivity (i.e., a larger δa), as illustrated in Fig. 7 by plotting δa as a function of momentum width Δk.

Comparing sensitivities of a MZ Interferometer and an Atomic FPI

Having determined the optimum cavity width d for each momentum width Δk, the device length L_t approximately given by the parameter L. We can now study the relationship between optimum Fisher information and length L.

In Fig. 8, we compare the sensitivity of an atomic FPI to a MZ interferometer of equivalent length L for three different momentum widths Δk. For a currently experimentally-achievable momentum width ($\Delta k = 0.025k_0$[126]), the MZ device achieves superior sensitivity. However, for an order of magnitude narrower momentum width ($\Delta k = 10^{-3}k_0$) an atomic FPI can compete with a MZ device for small lengths, and for an order of magnitude further ($\Delta k = 5\times 10^{-4}k_0$) the atomic FPI is more sensitive for $L < 0.2$ mm. Thus, the atomic FPI offers an effective compact alternative to an atom interferometer, which can improve the sensitivity further once cooling schemes can further narrow the momentum width of atomic clouds.

Discussion

We have investigated the application of an atomic FPI as a space-based acceleration sensor with a non-interacting pulsed BEC source. We used an analytic approximation for the transmission of the FPI, and showed this

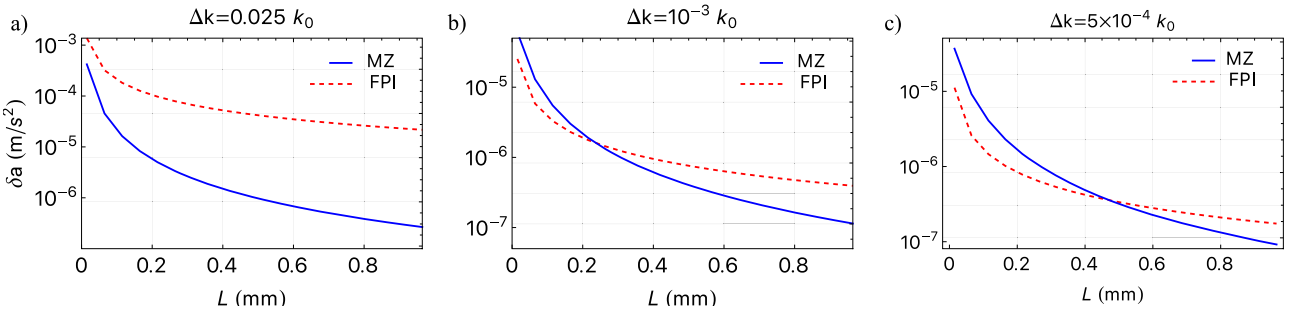

Fig. 8 | Plot comparing the acceleration sensitivity as a function of length L of an atomic FPI with that of a MZ interferometer, using a finite momentum width BEC source for a space based system ($a_0 \to 0$). a–c use $d\kappa = \{7.55, 26.1, 32.89\}$ and $k_i/\kappa = \{0.237, 0.106, 0.086\}$ respectively, which are the optimum values corresponding their specific momentum widths. Three plots compare the sensitivities using BECs with different momentum widths. For small device length and low momentum width, the sensitivity of an atomic FPI surpasses that of a MZ interferometer.

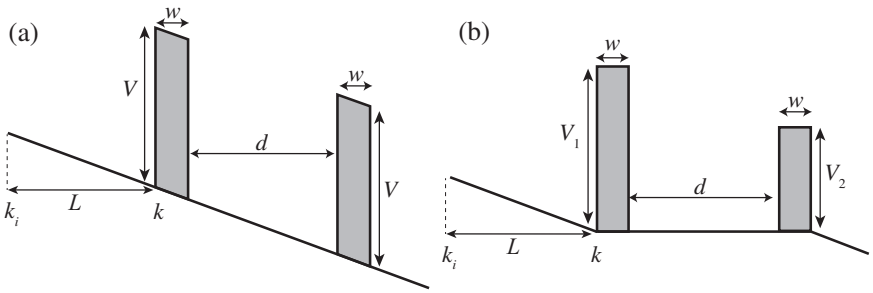

Fig. 9 | Accelerated atomic FPI: Schematic and simplified analytical model. a Schematic diagram of an atomic FPI made of two symmetric rectangular barriers in an accelerating field. **b** Simplified model, with an exact analytic solution, that approximates the system shown in (**a**). Here $\hbar k_i$ is the initial momentum of the particle, $\hbar k$ is the momentum of the particle at the position of the first barrier, after travelling a distance L, V_1 and V_2 are the heights of the first and second barriers respectively, w is the barrier width, and d is the cavity length.

expression agreed well with the exact transmission predicted by simulation of the Schrödinger equation. We quantified the sensitivity of the atomic FPI as an accelerometer using the classical Fisher information, and studied the sensitivity of FPIs with an atomic cloud source of both infinitely narrow and finite momentum width. In the case of an infinitely narrow momentum width source, an approximate expression for the optimum Fisher information and sensitivity was derived, and it was found that in the low length and high finesse regime an atomic FPI provided superior sensitivity to a MZ interferometer of equivalent total device length.

When a finite momentum width source is used, there is suppression of the transmission, particularly when the momentum width exceeds the linewidth of the cavity, leading to an optimal cavity width for maximum sensitivity. We demonstrated that the sentivity of the atomic FPI in the low device length regime is promising, and if a narrower momentum width can be realised, the atomic FPI could achieve greater sensitivity in the low length regime. Therefore, if atomic cooling techniques continue to advance in the coming years, the atomic FPI presents an exciting miniature accelerometer.

These results are a best-case scenario: we have assumed a non-interacting BEC, and have only worked in 1D. Detailed analysis of the uncertainty in the cavity length, barrier height, atom number and velocity of the atomic cloud are necessary in future work.

This work has focused on the atomic FPI as a space-based accelerometer. When applied as an earth-based accelerometer, the atomic cloud gains significantly more energy in the accelerating period before the first barrier. The barrier height must then be increased to exceed the atomic energy (a necessary condition for the atomic FPI to function), which necessitates a reduction in barrier width and cavity length as per the parameters determined in ref. 119. The barrier width required now is three orders of magnitude smaller than achievable by existing laser focusing methods. To overcome this difficulty, we propose an alternative scheme: initially position the atoms on the right hand side of the barrier in Fig. 9, and provide a momentum kick against the direction of the acceleration (towards the barriers). The acceleration will therefore reduce the energy of the atomic cloud, so that an experimentally feasible barrier width may be used.

Methods

Model

We consider the transmission of a beam of particles through an atomic Fabry-Perot 'cavity' made of two symmetric rectangular barriers in a uniform accelerating field (see Fig. 9a). We obtain a simplified model that is analytically tractable by making two assumptions. Firstly, we assume that the effect of acceleration within the barrier can be neglected. This assumption requires the barrier width (w) to be small compared to the distance between the initial particle positions and the first barrier (L). Secondly, we account for the acceleration potential energy the particles gain after travelling a distance $w + d$ through the first barrier and the cavity by reducing the energy of the second barrier by the particle's energy gain:

$$V_2(a) = V_1 - ma(w + d), \tag{13}$$

where m is the mass of each particle and a is acceleration (assumed to be uniform over device length $d + 2w$), V_1 and V_2 are the heights of the first and second barriers, respectively. These two simplifications give the double asymmetric rectangular barrier model shown in Fig. 9b.

Using this simplified model, we can analytically determine how acceleration affects transmission through the atomic FPI. We first consider the case of an incoming plane wave. If the initial momentum of the particle is $\hbar k_i$, then classically after travelling a distance L under uniform acceleration a, the particle's energy changes by maL. Since the BEC will be prepared a distance L from the first barrier, we therefore take the momentum of the plane wave incident on the asymmetric double barrier system to be

$$\hbar k(a) = \hbar k_i \sqrt{1 + \frac{2m^2 aL}{\hbar^2 k_i^2}}. \tag{14}$$

The probability of transmission through the double barrier system is given by the transmission coefficient[127]

$$T_{k_i}(a) = \frac{T_{\max}(a)}{1 + \left(\frac{2\mathcal{F}(a)}{\pi}\right)^2 \sin^2\left(k(a)d + \phi_a(a)\right)}, \tag{15}$$

where $T_{\max}(a)$ is the maximum achievable transmission coefficient, $\mathcal{F}(a)$ is the finesse of the atomic Fabry-Perot cavity and $\phi_a(a)$ is a phase shift that sets the resonance condition for the cavity. Our decision to denote the dependence of k_i explicitly will become clear shortly. In analogy with the optical Fabry-Perot cavity, the maximum transmission coefficient and finesse are most intuitively expressed in terms of the reflection coefficients of the two barriers (i.e., cavity 'mirrors'), $R_1(a)$ and $R_2(a)$. Explicitly,

$$T_{\max}(a) = 1 - \left[\frac{\sqrt{R_1(a)} - \sqrt{R_2(a)}}{1 - \sqrt{R_1(a)R_2(a)}}\right]^2, \tag{16}$$

$$\mathcal{F}(a) = \frac{\pi\left[R_1(a)R_2(a)\right]^{1/4}}{1 - \sqrt{R_1(a)R_2(a)}}, \tag{17}$$

where

$$R_j(a) = \frac{M_j^+(a)^2}{M_j^-(a)^2 + \coth^2\left[\beta_j(a)w\right]}, \tag{18}$$

with

$$\beta_1(a)^2 = \frac{2m}{\hbar^2}[V_1 - E(a)], \quad \beta_2(a)^2 = \frac{2m}{\hbar^2}[V_2(a) - E(a)], \tag{19a}$$

$$M_j^{\pm}(a) = \frac{1}{2}\left[\frac{\beta_j(a)}{k(a)} \pm \frac{k(a)}{\beta_j(a)}\right]. \tag{19b}$$

Here $E(a) = (\hbar k(a))^2/2m$ is the energy of the incident plane wave. The phase shift $\phi_a(a)$ similarly depends upon the cavity 'mirror' parameters:

$$\phi_a(a) = \frac{1}{2}\left[\pi - \left(\phi_1(a) + \phi_2(a)\right)\right], \tag{20}$$

where

$$\phi_j(a) = \tan^{-1}\left[M_j^- \tanh\left(\beta_j(a)w_j\right)\right], j = 1, 2. \tag{21}$$

The atomic system provides key differences compared to the well-known optical FPI, including atomic mass and mirrors where the key parameters can be tuned. Hence the transmission spectrum of an atomic FPI differs from that of an optical FPI in many ways. The reflectivity of optical potentials exhibits distinct behaviour compared to conventional mirrors, resulting in variations in reflectivity when scanning the momentum/energy of the source atoms. Hence, unlike the optical case, in the atomic analog scanning k and d are not equivalent. In section "Quantifying Acceleration Sensitivity", we analyze the effects of varying k and d separately to highlight their distinct influences. The width and contrast of the peaks in the transmission spectrum changes with change in wave number of the atomic source. Nevertheless, as we show below, in appropriately chosen regimes the transmission depends sensitively on the acceleration, allowing an atomic FPI to operate as a sensitive accelerometer.

It is straightforward to extend the above results to an incident atomic cloud of non-interacting atoms with a spread of momenta. Since the atoms do not interact, there is a one-to-one mapping between incoming and outgoing momentum. Consequently, the overall transmission is simply the integral over all transmission coefficients (indexed by incident wavevector k_i) weighted by the incident atomic cloud's k-space distribution $P(k_i)$:

$$T(a) = \int dk_i\, P(k_i) T_{k_i}(a). \tag{22}$$

We validate our analytic model by comparing to numeric simulation. In particular, we simulate the evolution of the Schrödinger equation for a non-interacting Gaussian BEC source, which we assume was in the ground state of a harmonic trapping potential of trapping frequency ω_z, before being released and interacting with the atomic Fabrey-Perot cavity, formed by external potential $V(z)$. The transmission coefficient T is computed as

$$T = \frac{N_T}{N_T + N_R}, \tag{23}$$

where N_T and N_R, the number of transmitted and reflected particles, are defined as

$$N_T = \int_{z_T}^{\infty} |\psi(z, t_{\text{end}})|^2\, dz, \tag{24a}$$

$$N_R = \int_{-\infty}^{z_R} |\psi(z, t_{\text{end}})|^2\, dz. \tag{24b}$$

The transmitted and reflected regions are specified as $z > z_T = z_0 + 3\sigma_c + L + d + 2w$ and $z < z_R = z_0 + 3\sigma_c + L$ respectively, where z_0 denotes the initial position of the atomic cloud. The stopping time, t_{end} is chosen so that there are no atoms left in the cavity; this is quantified by when N_T/N and N_R/N do not change by more than 10^{-6} in a given time step. Here, $N(t) = \int_{-\infty}^{\infty} dz\, |\psi(z,t)|^2$ is the normalisation of the wavefunction. The external potential used is given by $V(z) = V_b - maz$, where V_b is the potential generated by two barriers of width w and height V_1 separated by distance d. The simulation was completed using the open-source software package XMDS2[128] with an adaptive 4th–5th order Runge-Kutta interaction picture algorithm.

In Fig. 10a we plot the transmission coefficient calculated via Eq. (15) (black solid curve) and numeric simulation (red dotted curve) corresponding to a range of k_i/κ values, where κ is a momentum length scale determined by $\kappa = \sqrt{2mV_1/\hbar^2}$. We use the cavity parameters for ^{85}Rb determined in ref. 119 ($V_1 = 3.83 \times 10^{-32}$ J $= 5.81\, \hbar\omega_z$, $w = 1$ μm and $d = 4$ μm) with trapping frequency $\omega_z = 2\pi \times 10$ Hz in the presence of an acceleration of $a = 0$. Similarly, in Fig. 10b we plot the transmission coefficient for a fixed $k_i/\kappa = 0.45$ and varying a. In both instances, we observe that the curve corresponding to Eq. (15) matches the simulation data very well, validating the analytic model.

Now that we have an analytic function that connects transmission coefficient (T), reflection coefficient (R) and acceleration (a), we can invert that function to get acceleration from a measurement that provides us with an estimate of T and R. For a finite momentum width, the numeric relationship between T, R, and a can be used to calculate a using maximum likelihood estimation.

Quantifying acceleration sensitivity

The smallest change in acceleration (δa) detectable by an accelerometer quantifies the sensitivity of the device. For a cloud of N non-interacting, uncorrelated atoms, this is given by the Cramér-Rao bound[129]

$$\delta a = \frac{1}{\sqrt{NF_C(a)}}, \tag{25}$$

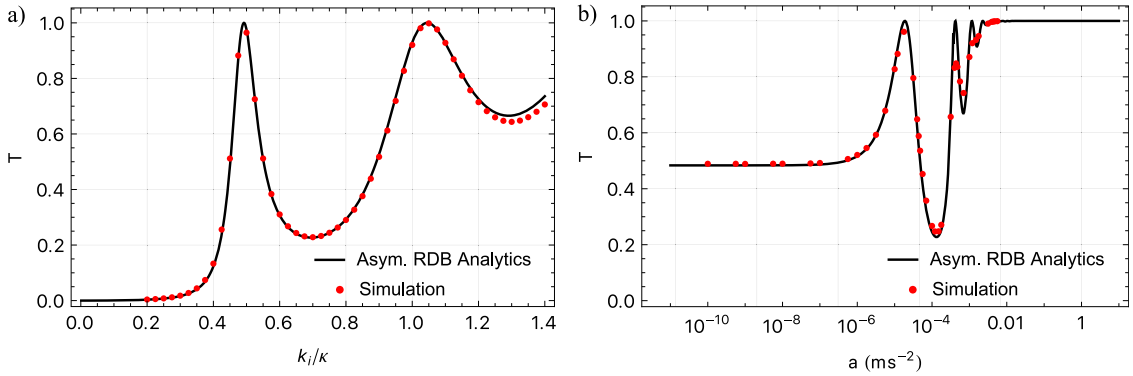

Fig. 10 | Comparison of analytic and simulated resonances in accelerated double-barrier transmission. Comparison of the analytic (black curve) and simulation (red dotted curve) results of transmission resonances of a beam of particles transmitting through double rectangular barriers in an accelerating field, for (**a**) a fixed acceleration $a = 0$ and varying initial momentum kick k_i/κ and (**b**) a fixed initial momentum kick $k_i/\kappa = 0.45$ and varying acceleration a. Here, the Schrödinger equation is simulated for a Gaussian cloud of a non-interacting BEC source. The parameters used for the simulation are: $V_1 = 3.83 \times 10^{-32} J$, $w = 1$ μm and $d = 4$ μm. For ^{85}Rb, the momentum scale $\kappa = \sqrt{2mV_1}/\hbar = 9.9 \times 10^6 \mathrm{m}^{-1}$. The external potential is given by $V(z) = V_b - maz$, where V_b is the double rectangular barrier potential. The analytical results agree well with the simulation result, validating the analytical model.

where $F_C(a)$ is the per-particle classical Fisher information[130,131], given by

$$F_C(a) = \sum_m \frac{(\partial \mathcal{P}_m/\partial a)^2}{\mathcal{P}_m(a)}. \tag{26}$$

Here $\mathcal{P}_m(a)$ is the probability distribution (indexed by m) constructed from measurements of a particular observable, and so $F_C(a)$ depends upon this choice of observable. For the atomic FPI considered in this work, we measure the number of transmitted and reflected atoms, yielding the transmission and reflection coefficients $T(a)$ and $R(a) = 1 - T(a)$, respectively. These coefficients are the probability distributions for transmission and reflection, respectively, that we need to compute the classical Fisher information:

$$\begin{aligned} F_C(a) &= \frac{(\partial T/\partial a)^2}{T(a)} + \frac{(\partial R/\partial a)^2}{R(a)} \\ &= \frac{(\partial T/\partial a)^2}{T(a)(1-T(a))}, \end{aligned} \tag{27}$$

where we have invoked $\partial R/\partial a = -\partial T/\partial a$. From Eq. (25), it follows that we should optimise for higher F_C, since that corresponds to a more sensitive accelerometer.

In our analysis we use dimensionless parameters with $1/\kappa$ as the unit of length and $\hbar\kappa$ as the unit of momentum, where $\kappa = \sqrt{(2mV_1/\hbar)}$ is the wave vector corresponding to the first barrier. Specifically, we define

$$\tilde{d} = \kappa d, \quad \tilde{L} = \kappa L, \quad \tilde{k} = k/\kappa, \tag{28}$$

$$\tilde{a} = \frac{2m^2 a}{\hbar^2 \kappa^3}, \quad \tilde{F}_C = \frac{F_C \hbar^4 \kappa^6}{4m^4}. \tag{29}$$

Data availability

The data that support the findings in this study are available on request.

Received: 8 November 2024; Accepted: 26 June 2025;
Published online: 07 July 2025

References

1. Canuel, B. et al. Six-axis inertial sensor using cold-atom interferometry. *Phys. Rev. Lett.* **97**, 010402 (2006).
2. Templier, S. et al. Tracking the vector acceleration with a hybrid quantum accelerometer triad. *Sci. Adv.* **8**, eadd3854 (2022).
3. Gustavson, T. L., Bouyer, P. & Kasevich, M. A. Precision rotation measurements with an atom interferometer gyroscope. *Phys. Rev. Lett.* **78**, 2046–2049 (1997).
4. Gustavson, T. L., Landragin, A. & Kasevich, M. A. Rotation sensing with a dual atom-interferometer Sagnac gyroscope. *Classical Quantum Gravity* **17**, 2385 (2000).
5. Durfee, D. S., Shaham, Y. K. & Kasevich, M. A. Long-term stability of an area-reversible atom-interferometer sagnac gyroscope. *Phys. Rev. Lett.* **97**, 240801 (2006).
6. Gauguet, A., Canuel, B., Lévèque, T., Chaibi, W. & Landragin, A. Characterization and limits of a cold-atom sagnac interferometer. *Phys. Rev. A* **80**, 063604 (2009).
7. Gautier, R. et al. Accurate measurement of the sagnac effect for matter waves. *Sci. Adv.* **8**, eabn8009 (2022).
8. Peters, A., Chung, K. Y. & Chu, S. Measurement of gravitational acceleration by dropping atoms. *Nature* **400**, 849–852 (1999).
9. Peters, A., Chung, K. Y. & Chu, S. High-precision gravity measurements using atom interferometry. *Metrologia* **38**, 25–61 (2001).
10. Altin, P. A. et al. Precision atomic gravimeter based on Bragg diffraction. *N. J. Phys.* **15**, 023009 (2013).
11. Hu, Z.-K. et al. Demonstration of an ultrahigh-sensitivity atom-interferometry absolute gravimeter. *Phys. Rev. A* **88**, 043610 (2013).
12. Farah, T. et al. Underground operation at best sensitivity of the mobile lne-syrte cold atom gravimeter. *Gyroscopy Navig.* **5**, 266–274 (2014).
13. Hardman, K. S. et al. Simultaneous precision gravimetry and magnetic gradiometry with a bose-einstein condensate: a high precision, quantum sensor. *Phys. Rev. Lett.* **117**, 138501 (2016).
14. Zhang, T. et al. Ultrahigh-sensitivity bragg atom gravimeter and its application in testing lorentz violation. *Phys. Rev. Appl.* **20**, 014067 (2023).
15. Snadden, M. J., McGuirk, J. M., Bouyer, P., Haritos, K. G. & Kasevich, M. A. Measurement of the earth's gravity gradient with an atom interferometer-based gravity gradiometer. *Phys. Rev. Lett.* **81**, 971–974 (1998).
16. Sorrentino, F. et al. Sensitivity limits of a Raman atom interferometer as a gravity gradiometer. *Phys. Rev. A* **89**, 023607 (2014).
17. Biedermann, G. W. et al. Testing gravity with cold-atom interferometers. *Phys. Rev. A* **91**, 033629 (2015).
18. D'Amico, G. et al. Bragg interferometer for gravity gradient measurements. *Phys. Rev. A* **93**, 063628 (2016).
19. Asenbaum, P. et al. Phase shift in an atom interferometer due to spacetime curvature across its wave function. *Phys. Rev. Lett.* **118**, 183602 (2017).
20. Janvier, C. et al. Compact differential gravimeter at the quantum projection-noise limit. *Phys. Rev. A* **105**, 022801 (2022).

21. Parker, R. H., Yu, C., Zhong, W., Estey, B. & Müller, H. Measurement of the fine-structure constant as a test of the standard model. *Science* **360**, 191–195 (2018).
22. Yu, C. et al. Atom-interferometry measurement of the fine structure constant. *Ann. der Phys.* **531**, 1800346 (2019).
23. Morel, L., Yao, Z., Cladé, P. & Guellati-Khélifa, S. Determination of the fine-structure constant with an accuracy of 81 parts per trillion. *Nature* **588**, 61–65 (2020).
24. Rosi, G., Sorrentino, F., Cacciapuoti, L., Prevedelli, M. & Tino, G. M. Precision measurement of the newtonian gravitational constant using cold atoms. *Nature* **510**, 518–521 (2014).
25. Jekeli, C. Navigation error analysis of atom interferometer inertial sensor. *Navigation* **52**, 1–14 (2005).
26. Battelier, B. et al. Development of compact cold-atom sensors for inertial navigation. in *Quantum Optics,* (eds. Stuhler, J. & Shields, A. J.) 21 – 37 (SPIE, 2016).
27. Narducci, F. A., Black, A. T. & Burke, J. H. Advances toward fieldable atom interferometers. *Adv. Phys. X* **7**, 1946426 (2022).
28. Wang, X. et al. Enhancing inertial navigation performance via fusion of classical and quantum accelerometers. *arXiv:2103.09378 [physics, physics:quant-ph]*. http://arxiv.org/abs/2103.09378 (2021).
29. Wright, M. J. et al. Cold atom inertial sensors for navigation applications. *Front. Phys.* **10**, 994459 (2022).
30. Phillips, A. M. et al. Position fixing with cold atom gravity gradiometers. *AVS Quantum Sci.* **4**, 024404 (2022).
31. Metje, N., Chapman, D. N., Rogers, C. D. F. & Bongs, K. Seeing through the ground: the potential of gravity gradient as a complementary technology. *Adv. Civ. Eng.* **2011**, e903758 (2011).
32. Boddice, D., Metje, N. & Tuckwell, G. Capability assessment and challenges for quantum technology gravity sensors for near surface terrestrial geophysical surveying. *J. Appl. Geophys.* **146**, 149–159 (2017).
33. Stray, B. et al. Quantum sensing for gravity cartography. *Nature* **602**, 590–594 (2022).
34. van Leeuwen, E. H. BHP develops airborne gravity gradiometer for mineral exploration. *Lead. Edge* **19**, 1296–1297 (2000).
35. Bongs, K. et al. Taking atom interferometric quantum sensors from the laboratory to real-world applications. *Nat. Rev. Phys.* **1**, 731–739 (2019).
36. Schilling, M. et al. Gravity field modelling for the Hannover 10 m atom interferometer. *J. Geod.* **94**, 122 (2020).
37. Stockton, J. K., Takase, K. & Kasevich, M. A. Absolute geodetic rotation measurement using atom interferometry. *Phys. Rev. Lett.* **107**, 133001 (2011).
38. Migliaccio, F. et al. Mocass: a satellite mission concept using cold atom interferometry for measuring the earth gravity field. *Surv. Geophys.* **40**, 1029–1053 (2019).
39. Trimeche, A. et al. Concept study and preliminary design of a cold atom interferometer for space gravity gradiometry. *Classical Quantum Gravity* **36**, 215004 (2019).
40. Lévèque, T. et al. Gravity field mapping using laser-coupled quantum accelerometers in space. *J. Geod.* **95**, 15 (2021).
41. Bidel, Y. et al. Absolute marine gravimetry with matter-wave interferometry. *Nat. Commun.* **9**, 627 (2018).
42. Wu, B. et al. Marine absolute gravity field surveys based on cold atomic gravimeter. *IEEE Sens. J.* **23**, 24292–24299 (2023).
43. Geiger, R. et al. Detecting inertial effects with airborne matter-wave interferometry. *Nat. Commun.* **2**, https://doi.org/10.1038/ncomms1479 (2011).
44. Bidel, Y. et al. Absolute airborne gravimetry with a cold atom sensor. *J. Geod.* **94**, 20 (2020).
45. Bidel, Y. et al. Airborne absolute gravimetry with a quantum sensor, comparison with classical technologies. *J. Geophys. Res. Solid Earth* **128**, e2022JB025921 (2023).
46. Becker, D. et al. Space-borne Bose–Einstein condensation for precision interferometry. *Nature* **562**, 391–395 (2018).
47. Lachmann, M. D. et al. Ultracold atom interferometry in space. *Nat. Commun.* **12**, 1317 (2021).
48. Williams, J. R. et al. Pathfinder experiments with atom interferometry in the Cold Atom Lab onboard the International Space Station. *Nat. Commun.* **15**, 6414 (2024).
49. Dimopoulos, S., Graham, P. W., Hogan, J. M., Kasevich, M. A. & Rajendran, S. Atomic gravitational wave interferometric sensor. *Phys. Rev. D.* **78**, 122002 (2008).
50. Dimopoulos, S., Graham, P. W., Hogan, J. M. & Kasevich, M. A. Testing general relativity with atom interferometry. *Phys. Rev. Lett.* **98**, 111102 (2007).
51. Williams, J., Chiow, S.-w, Yu, N. & Müller, H. Quantum test of the equivalence principle and space-time aboard the International Space Station. *N. J. Phys.* **18**, 025018 (2016).
52. Burrage, C. & Copeland, E. J. Using atom interferometry to detect dark energy. *Contemp. Phys.* **57**, 164–176 (2016).
53. Sabulsky, D. O. et al. Experiment to detect dark energy forces using atom interferometry. *Phys. Rev. Lett.* **123**, 061102 (2019).
54. Geraci, A. A. & Derevianko, A. Sensitivity of atom interferometry to ultralight scalar field dark matter. *Phys. Rev. Lett.* **117**, 261301 (2016).
55. Badurina, L. et al. AION: an atom interferometer observatory and network. *J. Cosmol. Astropart. Phys.* **2020**, 011–011 (2020).
56. Haine, S. A. Searching for signatures of quantum gravity in quantum gases. *N. J. Phys.* **23**, 033020 (2021).
57. Margalit, Y. et al. Realization of a complete Stern-Gerlach interferometer: toward a test of quantum gravity. *Sci. Adv.* **7**, eabg2879 (2021).
58. HosseiniArani, A. et al. Advances in atom interferometry and their impacts on the performance of quantum accelerometers on-board future satellite gravity missions. *Adv. Space Res.* **74**, 3186–3200 (2024).
59. Abe, M. et al. Matter-wave atomic gradiometer interferometric sensor (magis-100). *Quantum Sci. Technol.* **6**, 044003 (2021).
60. Fang, B. et al. Metrology with atom interferometry: inertial sensors from laboratory to field applications. *J. Phys. Conf. Ser.* **723**, 012049 (2016).
61. Geiger, R., Landragin, A., Merlet, S. & Pereira Dos Santos, F. High-accuracy inertial measurements with cold-atom sensors. *AVS Quantum Sci.* **2**, 024702 (2020).
62. Cladé, P., Guellati-Khélifa, S., Nez, Fmc & Biraben, Fmc Large momentum beam splitter using Bloch oscillations. *Phys. Rev. Lett.* **102**, 240402 (2009).
63. Müller, H., Chiow, S.-w, Long, Q., Herrmann, S. & Chu, S. Atom interferometry with up to 24-photon-momentum-transfer beam splitters. *Phys. Rev. Lett.* **100**, 180405 (2008).
64. Chiow, S.-w, Kovachy, T., Chien, H.-C. & Kasevich, M. A. 102$\hbar k$ large area atom interferometers. *Phys. Rev. Lett.* **107**, 130403 (2011).
65. McDonald, G. D. et al. 80$\hbar k$ momentum separation with bloch oscillations in an optically guided atom interferometer. *Phys. Rev. A* **88**, 053620 (2013).
66. Kotru, K., Butts, D. L., Kinast, J. M. & Stoner, R. E. Large-area atom interferometry with frequency-swept raman adiabatic passage. *Phys. Rev. Lett.* **115**, 103001 (2015).
67. Gebbe, M. et al. Twin-lattice atom interferometry. *Nat. Commun.* **12**, 2544 (2021).
68. Wilkason, T. et al. Atom interferometry with floquet atom optics. *Phys. Rev. Lett.* **129**, 183202 (2022).
69. Béguin, A., Rodzinka, T., Calmels, L., Allard, B. & Gauguet, A. Atom interferometry with coherent enhancement of bragg pulse sequences. *Phys. Rev. Lett.* **131**, 143401 (2023).
70. Debs, J. E. et al. Cold-atom gravimetry with a Bose-Einstein condensate. *Phys. Rev. A* **84**, 033610 (2011).
71. Robins, N. P., Altin, P. A., Debs, J. E. & Close, J. D. Atom lasers: production, properties and prospects for precision inertial measurement. *Phys. Rep.* **529**, 265–296 (2013).

72. Szigeti, S. S., Debs, J. E., Hope, J. J., Robins, N. P. & Close, J. D. Why momentum width matters for atom interferometry with Bragg pulses. *N. J. Phys.* **14**, 023009 (2012).
73. Deppner, C. et al. Collective-mode enhanced matter-wave optics. *Phys. Rev. Lett.* **127**, 100401 (2021).
74. Hensel, T. et al. Inertial sensing with quantum gases: a comparative performance study of condensed versus thermal sources for atom interferometry. *Eur. Phys. J. D.* **75**, 108 (2021).
75. Chen, C.-C. et al. Continuous bose–einstein condensation. *Nature* **606**, 683–687 (2022).
76. Lee, J. et al. A compact cold-atom interferometer with a high data-rate grating magneto-optical trap and a photonic-integrated-circuit-compatible laser system. *Nat. Commun.* **13**, 5131 (2022).
77. Wigley, P. B. et al. Readout-delay-free Bragg atom interferometry using overlapped spatial fringes. *Phys. Rev. A* **99**, 023615 (2019).
78. Piccon, R., Sarkar, S., Gomes Baptista, J., Merlet, S. & Pereira Dos Santos, F. Separating the output ports of a bragg interferometer via velocity selective transport. *Phys. Rev. A* **106**, 013303 (2022).
79. Ben-Aïcha, Y. et al. A dual open atom interferometer for compact, mobile quantum sensing. https://arxiv.org/abs/2405.00400 (2024).
80. Saywell, J., Carey, M., Belal, M., Kuprov, I. & Freegarde, T. Optimal control of raman pulse sequences for atom interferometry. *J. Phys. B At. Mol. Opt. Phys.* **53**, 085006 (2020).
81. Saywell, J. C. et al. Enhancing the sensitivity of atom-interferometric inertial sensors using robust control. *Nat. Commun.* **14**, 7626 (2023).
82. Realizing software-defined quantum sensing: experimental demonstration of software-ruggedized atom interferometry for mobile quantum inertial sensing, **12447**. https://doi.org/10.1117/12.2657269
83. Wang, Y. et al. Robust quantum control via multipath interference for thousandfold phase amplification in a resonant atom interferometer. *Phys. Rev. Lett.* **133**, 243403 (2024).
84. Rodzinka, T. et al. Optimal floquet state engineering for large scale atom interferometers. *Nat Commun* **15**, 10281 (2024).
85. Estève, J., Gross, C., Weller, A., Giovanazzi, S. & Oberthaler, M. K. Squeezing and entanglement in a Bose–Einstein condensate. *Nature* **455**, 1216–1219 (2008).
86. Appel, J. et al. Mesoscopic atomic entanglement for precision measurements beyond the standard quantum limit. *Proc. Natl Acad. Sci. USA* **106**, 10960–10965 (2009).
87. Lücke, B. et al. Twin matter waves for interferometry beyond the classical limit. *Science* **334**, 773–776 (2011).
88. Haine, S. A. & Ferris, A. J. Surpassing the standard quantum limit in an atom interferometer with four-mode entanglement produced from four-wave mixing. *Phys. Rev. A* **84**, 043624 (2011).
89. Hamley, C. D., Gerving, C. S., Hoang, T. M., Bookjans, E. M. & Chapman, M. S. Spin-nematic squeezed vacuum in a quantum gas. *Nat. Phys.* **8**, 305–308 (2012).
90. Lücke, B. et al. Detecting multiparticle entanglement of dicke states. *Phys. Rev. Lett.* **112**, 155304 (2014).
91. Muessel, W. et al. Twist-and-turn spin squeezing in Bose-Einstein condensates. *Phys. Rev. A* **92**, 023603 (2015).
92. Lange, K. et al. Entanglement between two spatially separated atomic modes. *Science* **360**, 416–418 (2018).
93. Szigeti, S. S., Nolan, S. P., Close, J. D. & Haine, S. A. High-precision quantum-enhanced gravimetry with a Bose-Einstein condensate. *Phys. Rev. Lett.* **125**, 100402 (2020).
94. Szigeti, S. S., Hosten, O. & Haine, S. A. Improving cold-atom sensors with quantum entanglement: prospects and challenges. *Appl. Phys. Lett.* **118**, 140501 (2021).
95. Hald, J., Sørensen, J. L., Schori, C. & Polzik, E. S. Spin squeezed atoms: a macroscopic entangled ensemble created by light. *Phys. Rev. Lett.* **83**, 1319–1322 (1999).
96. Leroux, I. D., Schleier-Smith, M. H. & Vuletić, V. Implementation of cavity squeezing of a collective atomic spin. *Phys. Rev. Lett.* **104**, 073602 (2010).
97. Schleier-Smith, M. H., Leroux, I. D. & Vuletić, V. Squeezing the collective spin of a dilute atomic ensemble by cavity feedback. *Phys. Rev. A* **81**, 021804 (2010).
98. Sewell, R. J. et al. Magnetic sensitivity beyond the projection noise limit by spin squeezing. *Phys. Rev. Lett.* **109**, 253605 (2012).
99. Haine, S. A. Information-recycling beam splitters for quantum enhanced atom interferometry. *Phys. Rev. Lett.* **110**, 053002 (2013).
100. Szigeti, S. S., Tonekaboni, B., Lau, W. Y. S., Hood, S. N. & Haine, S. A. Squeezed-light-enhanced atom interferometry below the standard quantum limit. *Phys. Rev. A* **90**, 063630 (2014).
101. Haine, S. A. & Lau, W. Y. S. Generation of atom-light entanglement in an optical cavity for quantum enhanced atom interferometry. *Phys. Rev. A* **93**, 023607 (2016).
102. Kritsotakis, M., Dunningham, J. A. & Haine, S. A. Spin squeezing of a Bose-Einstein condensate via a quantum nondemolition measurement for quantum-enhanced atom interferometry. *Phys. Rev. A* **103**, 023318 (2021).
103. Fuderer, L. A., Hope, J. J. & Haine, S. A. Hybrid method of generating spin-squeezed states for quantum-enhanced atom interferometry. *Phys. Rev. A* **108**, 043722 (2023).
104. Drever, R. W. P. et al. Laser phase and frequency stabilization using an optical resonator. *Appl. Phys. B* **31**, 97–105 (1983).
105. Deventer, M. O. V., Spano, P. & Nielsen, S. K. Comparison of DFB laser linewidth measurement techniques: results from COST 215 round robin. *Electron. Lett.* **26**, 2018–2020 (1990).
106. Xue, J. et al. Pulsed laser linewidth measurement using Fabry–Pérot scanning interferometer. *Results Phys.* **6**, 698–703 (2016).
107. Yoshino, T., Kurosawa, K., Itoh, K. & Ose, T. Fiber-optic Fabry-Perot interferometer and its sensor applications. *IEEE Trans. Microw. Theory Tech.* **30**, 1612–1621 (1982).
108. Taylor, H. Principles and applications of fiber-optic Fabry-Perot sensors. In *Technical Digest. Summaries of Papers Presented at the Conference on Lasers and Electro-Optics. Conference Edition. 1998 Technical Digest Series,* (IEEE, 1998).
109. Carusotto, I. Nonlinear atomic Fabry-Perot interferometer: from the mean-field theory to the atom blockade effect. *Phys. Rev. A* **63**, 023610 (2001).
110. Paul, T., Richter, K. & Schlagheck, P. Nonlinear resonant transport of Bose-Einstein condensates. *Phys. Rev. Lett.* **94**, 020404 (2005).
111. Paul, T., Hartung, M., Richter, K. & Schlagheck, P. Nonlinear transport of Bose-Einstein condensates through mesoscopic waveguides. *Phys. Rev. A* **76**, 063605 (2007).
112. Rapedius, K. & Korsch, H. J. Barrier transmission for the one-dimensional nonlinear Schr\textbackslash"odinger equation: resonances and transmission profiles. *Phys. Rev. A* **77**, 063610 (2008).
113. Ernst, T., Paul, T. & Schlagheck, P. Transport of ultracold Bose gases beyond the Gross-Pitaevskii description. *Phys. Rev. A* **81**, 013631 (2010).
114. Dutt, A. & Kar, S. Smooth double barriers in quantum mechanics. *Am. J. Phys.* **78**, 1352–1360 (2010).
115. Damon, F., Vermersch, F., Muga, J. G. & Guéry-Odelin, D. Reduction of local velocity spreads by linear potentials. *Phys. Rev. A* **89**, 053626 (2014).
116. Wilkens, M., Goldstein, E., Taylor, B. & Meystre, P. Fabry-Perot interferometer for atoms. *Phys. Rev. A* **47**, 2366–2369 (1993).
117. Ruschhaupt, A., Delgado, F. & Muga, J. G. Velocity selection of ultra-cold atoms with Fabry–Perot laser devices: improvements and limits. *J. Phys. B At. Mol. Opt. Phys.* **38**, 2665–2674 (2005).
118. Valagiannopoulos, C. Quantum Fabry-Perot resonator: extreme angular selectivity in matter-wave tunneling. *Phys. Rev. Appl.* **12**, 054042 (2019).
119. Manju, P. et al. An atomic Fabry–Perot interferometer using a pulsed interacting Bose–Einstein condensate. *Sci. Rep.* **10**, 15052 (2020).

120. Roberts, J. L. et al. Resonant magnetic field control of elastic scattering in cold ^{85}*rb*. *Phys. Rev. Lett.* **81**, 5109–5112 (1998).
121. Kuhn, C. C. N. et al. A bose-condensed, simultaneous dual-species mach–zehnder atom interferometer. *N. J. Phys.* **16**, 073035 (2014).
122. Everitt, P. J. et al. Observation of a modulational instability in bose-einstein condensates. *Phys. Rev. A* **96**, 041601 (2017).
123. Eid, R., Hammond, A., Lavoine, L. & Bourdel, T. Ultracold-atom quantum tunneling through single and double optical barriers. *Phys. Rev. A* **110**, 043316 (2024).
124. Schach, P., Friedrich, A., Williams, J. R., Schleich, W. P. & Giese, E. Tunneling gravimetry. *EPJ Quantum Technol.* **9**, 1–19 (2022).
125. Freise, A. & Kenneth, S. Interferometer techniques for gravitational-wave detection. *Living Rev. Relativ* **13**, 47–48 (2010).
126. Kovachy, T. et al. Matter wave lensing to picokelvin temperatures. *Phys. Rev. Lett.* **114**, 143004 (2015).
127. Xiao, Z., Huang, H. & Lu, X.-X. Resonant tunneling dynamics and the related tunneling time. *Int. J. Mod. Phys. B* **29**, 1550052 (2015).
128. Dennis, G. R., Hope, J. J. & Johnsson, M. T. XMDS2: fast, scalable simulation of coupled stochastic partial differential equations. *Comput. Phys. Commun.* **184**, 201–208 (2013).
129. Tóth, G. & Apellaniz, I. Quantum metrology from a quantum information science perspective. *J. Phys. A Math. Theor.* **47**, 424006 (2014).
130. Haine, S. A. Mean-Field dynamics and fisher information in matter wave interferometry. *Phys. Rev. Lett.* **116**, 230404 (2016).
131. Kritsotakis, M., Szigeti, S. S., Dunningham, J. A. & Haine, S. A. Optimal matter-wave gravimetry. *Phys. Rev. A* **98**, 023629 (2018).

Acknowledgements

S.A.H. acknowledges support through an Australian Research Council Future Fellowship Grant No. FT210100809. SSS was supported by an Australian Research Council Discovery Early Career Researcher Award (DECRA), Project No. DE200100495. This research was undertaken with the assistance of resources and services from the National Computational Infrastructure (NCI), which is supported by the Australian Government.

Author contributions

The theoretical analysis and numerical simulations were carried out by M.P. under the supervision of S.S.S. and S.A.H., and M.J.B. contributed to the interpretation of the results and the writing of the manuscript.

Competing interests

The authors declare no competing interests.

Additional information

Correspondence and requests for materials should be addressed to Manju Perumbil.

Reprints and permissions information is available at http://www.nature.com/reprints

Publisher's note Springer Nature remains neutral with regard to jurisdictional claims in published maps and institutional affiliations.

Open Access This article is licensed under a Creative Commons Attribution-NonCommercial-NoDerivatives 4.0 International License, which permits any non-commercial use, sharing, distribution and reproduction in any medium or format, as long as you give appropriate credit to the original author(s) and the source, provide a link to the Creative Commons licence, and indicate if you modified the licensed material. You do not have permission under this licence to share adapted material derived from this article or parts of it. The images or other third party material in this article are included in the article's Creative Commons licence, unless indicated otherwise in a credit line to the material. If material is not included in the article's Creative Commons licence and your intended use is not permitted by statutory regulation or exceeds the permitted use, you will need to obtain permission directly from the copyright holder. To view a copy of this licence, visit http://creativecommons.org/licenses/by-nc-nd/4.0/.

© The Author(s) 2025